Available online at www.sciencedirect.com
ScienceDirect
Journal of Non-Crystalline Solids 353 (2007) 4707–4717
JOURNAL OF NON-CRYSTALLINE SOLIDS
www.elsevier.com/locate/jnoncrysol

Effect of microstructures on the compressive deformation and fracture behaviors of $Zr_{47}Cu_{46}Al_7$ bulk metallic glass composites

J.T. Fan [a], F.F. Wu [a], Z.F. Zhang [a,*], F. Jiang [b], J. Sun [b], S.X. Mao [a,c]

[a] *Shenyang National Laboratory for Materials Science, Institute of Metal Research, The Chinese Academy of Science, Shenyang 110016, People's Republic of China*
[b] *State Key Laboratory for Mechanical Behavior of Materials, Xi'an Jiaotong University, Xi'an 710049, People's Republic of China*
[c] *Department of Mechanical Engineering, University of Pittsburgh, Pittsburgh, PA 15261, USA*

Received 16 April 2007; received in revised form 22 June 2007
Available online 8 August 2007

Abstract

The compressive deformation and fracture behaviors of a $Zr_{47}Cu_{46}Al_7$ bulk metallic glass (BMG) and its composites with different microstructures were investigated. For the fully amorphous alloy, due to the formation of coarse primary shear bands and multiple secondary shear bands, it exhibited a high plasticity up to 14.5% with a 'work softening' during compressive test. With the increase in the volume fraction of primary crystallizing phases, the BMG composites displayed low strength and poor plasticity even failing in a brittle mode. Furthermore, the effects of microstructures on the compressive deformation and fracture behaviors of the BMG composites were discussed.

PACS: 62.20.Fe; 81.05.Kf; 62.20.Mk

Keywords: Amorphous metals; Metallic glasses; Alloys

1. Introduction

Bulk metallic glasses (BMGs) have been fabricated in many alloy systems [1–9], which has attracted tremendous attention [4–11]. At the same time, they are also considered for potential application in many commercial industries because of their high strength, excellent corrosion resistance and better physical and chemical properties compared with traditional crystalline alloys [12,13]. But unfortunately, the brittleness blocks largely their development. So recently, there has been considerable scientific and industrial interest in a variety of bulk metallic glass (BMG) composites as an effective way of further improving mechanical properties [14–22]. In these composites, the second phase hinders a single shear band from extending a critically through the whole sample at the onset of plastic deformation and seeds the initiation of multiple shear bands. The additive elements with high melting point, such as Ta, Nb, or Mo were added to Zr-, Cu-, and Ti-based BMGs by in situ precipitation of ductile micrometer-sized particles [16,17], bcc-β dendrites [18,19] or nanostructure-dendrites [20,21] upon cooling from the melting to improve the ductility of the composites. Most importantly, the perfect composition design must ensure high glass forming ability (GFA) which is necessary for the formation of bulk amorphous matrix and introduction of appropriate primary crystallizing phases. Therefore, the size, geometry and volume fraction of the primary crystallizing phase are also crucial for efficiently improving the mechanical properties. Many efforts have been devoted to investigate the effect of alloy element addition on the microstructure and volume fraction of primary crystallizing phase [20–22]. However, there are few results [23] about

* Corresponding author. Tel.: +86 24 23971043.
E-mail addresses: jtfan@imr.ac.cn (J.T. Fan), zhfzhang@imr.ac.cn (Z.F. Zhang).

0022-3093/$ - see front matter © 2007 Published by Elsevier B.V.
doi:10.1016/j.jnoncrysol.2007.06.062

the effect of microstructures and volume fraction of primary crystallizing phases on the deformation and fracture behaviors of an identical alloy under different cooling rates upon solidification.

Recently, it was reported that Zr–Cu–Al (or Cu–Zr–Al) ternary alloy has a better combination of high strength, good ductility and low production cost compared with the former Zr-, Cu- and Ti-based BMG composites [14–22]. It was shown that $Cu_{47.5}Zr_{47.5}Al_5$ BMG rod of 2 mm in diameter exhibited high compressive strength up to 2265 MPa together with 'work hardening' and large plastic strain of 18% [24]. Besides, plasticity-improved Zr–Cu–Al BMG matrix composites were also prepared by in situ precipitation of CuZr martensite phase [25]. However, the Zr–Cu–Al BMG and its composites were seldom larger than 4 mm in diameter which limited their application as structural materials.

In this paper, a $Zr_{47}Cu_{46}Al_7$ alloy is cast into a copper mold with a wedge shape whose thickness is up to 9 mm. The different thickness of the bulk samples leads to varying cooling rates upon solidification, which results in different microstructures and volume fraction of primary crystallizing phase. Furthermore, it is convenient to compare the mechanical properties of such metallic glass composites with varying microstructure and reveal the corresponding deformation and fracture behaviors.

2. Experimental procedures

In the present work, the alloy ingots with a nominal composition of $Zr_{47}Cu_{46}Al_7$ (at.%), were prepared by arc melting mixtures of ultrasonically cleansed Zr (crystal bar, 99.9 at.%), Cu (99.99 at.%) and Al (99.99 at.%) pieces, and the arc melting was performed in a Ti-gettered high purity argon atmosphere. At the same time, the electromagnetic stirring function was introduced to the equipment in order to make the elements more homogeneous by adding a current loop under the water-cooled copper crucible [26]. Each ingot was re-melted at least four times in order to ensure the chemical homogeneity. And then by copper mold casting, the ingots were cast into a wedge-shaped plate with a dimension of $90 \times 30 \times T\ mm^3$ (T ranges from 2 to 9). The variation of thickness, T, led to different cooling rates upon solidification for the as-cast BMG plate.

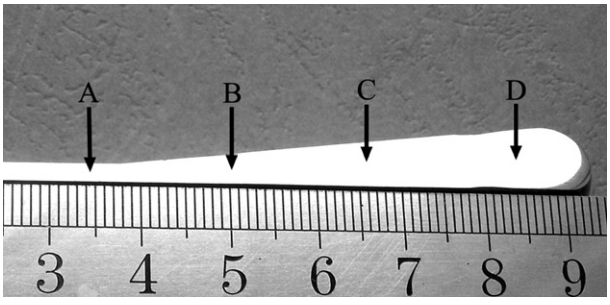

Fig. 1. As-cast $Zr_{47}Cu_{46}Al_7$ alloy wedge-shaped plate designating samples A, B, C and D.

Four groups of samples were cut from the centers of the four different positions with the thicknesses of 2.3, 4.2, 6.4 and 8.3 mm, respectively, and defined them as the samples A, B, C and D (Fig. 1). Each group had three samples for the compressive test and the average result was calculated from the three compressive stress–strain curves.

Firstly, all the samples were machined and polished into rectangular bars with the same dimension of $2 \times 2 \times 4\ mm^3$ for the compressive test. Simultaneously, one sample from each group was etched with hydrofluoric acid so as to expose the microstructure. Secondly, one typical sample from each group was analyzed by X-ray diffraction (XRD) using a Rigaku diffractometer with Cu-K_α radiation as a source and a Perkin–Elmer differential scanning calorimeter (DSC-7) under flowing purified argon with 600 °C rod at a heating rate of 60 K/min. At the same time, the microstructure characterization of sample A was observed by using a transition electron microscope (TEM; JEM-2000FXII) at 200 kV. And then, the compressive deformation was conducted on a computed-controlled, servo-hydraulic MTS-810 testing machine at a strain rate of $5 \times 10^{-4}\ s^{-1}$ at room temperature. Finally, the deformation and fracture morphologies on the side surfaces and fractographies were observed by using a Quanta-600 scanning electron microscope (SEM).

3. Results

3.1. Microstructures and in situ formed phases

The microstructures observed on the etched side surfaces of samples A, B, C and D using SEM are shown in Fig. 2. The featureless image of sample A gives no hint for any visible crystallization phase (Fig. 2(a)). The TEM selected area diffraction (SAD) pattern of sample A is clearly presented and inserted in Fig. 2(a). Also Fig. 3 shows the corresponding XRD patterns recorded from the cross-section of the as-cast alloys of samples A, B, C and D. The XRD pattern of sample A consists of only a series of broad diffraction maxima without any detectable sharp Bragg peaks, indicating that the microstructure is fully amorphous glass [27]. It was reported that the ratio of the maximum casting plate thickness L_{plate} to the rod diameter L_{rod} follows the relation: L_{plate}:L_{rod} = 1:1.7 [28]. So for sample A, the 2.3 mm thick plate is equivalent to the 3.9 mm rod in diameter processed by the same copper mold method, which is slightly larger than the reported thickness of 3.5 mm [29], indicating that the GFA can be improved if applying the suitable process technology. In a word, according to the results of SEM, TEM observations and XRD patterns, it can be undoubtedly concluded that sample A has a fully amorphous structure.

However, with decreasing cooling rate upon solidification, some primary crystallizing phases began to appear. Fig. 3 shows a few of 'spikes' detected on the XRD patterns of samples B, C and D, indicating that some primary crystallizing phases have precipitated with the increase in

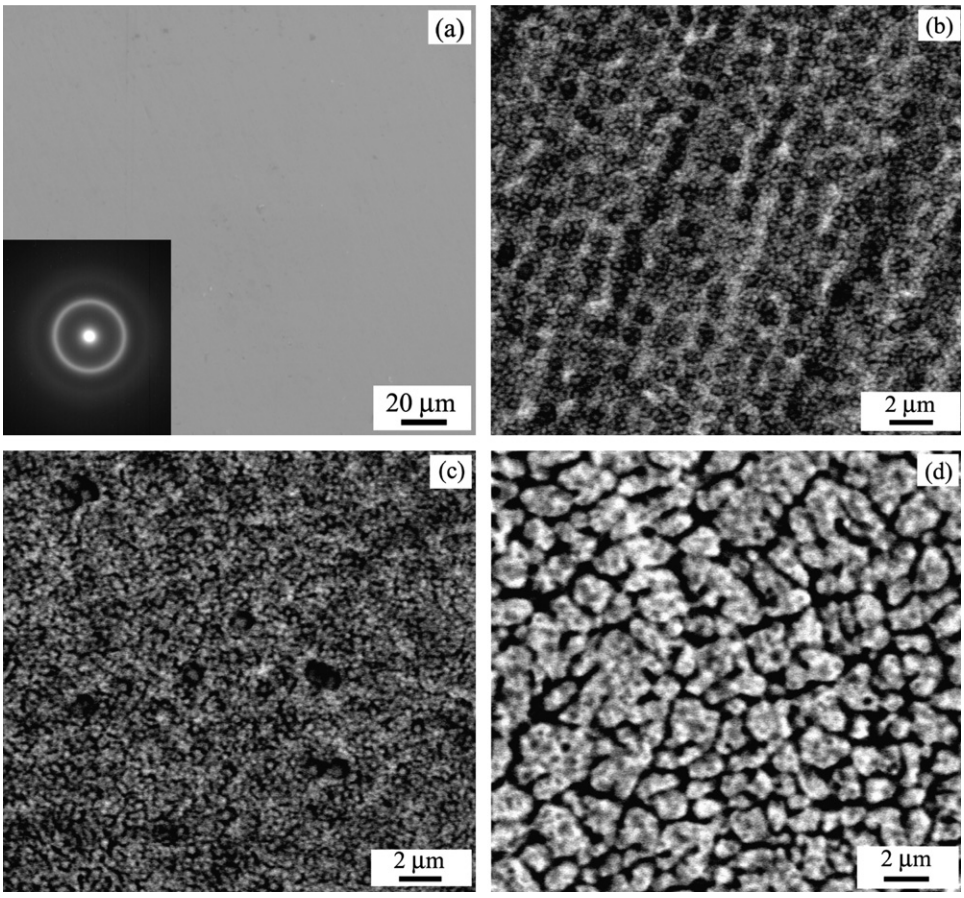

Fig. 2. SEM images of surfaces etched by hydrofluoric acid in the center of the cross-sectional areas of $Zr_{47}Cu_{46}Al_7$ alloy for (a) sample A, the inset shows its TEM selected area diffraction patterns and (b–d) samples B, C and D.

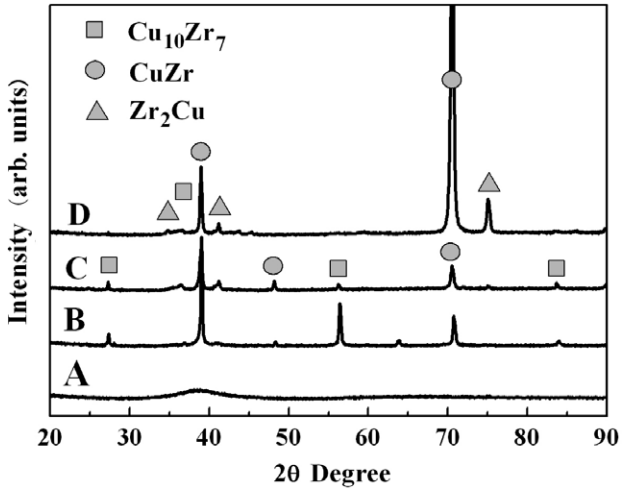

Fig. 3. XRD patterns of $Zr_{47}Cu_{46}Al_7$ alloy for samples A, B, C and D.

the thickness of the plate. For sample B, Fig. 2(b) shows that there are many dispersing small particles, implying the appearance of primary crystallizing phases. And for the metallic glass matrix, due to its high corrosion resistance, it remains unchanged after etching and forms some limited boundaries like 'fencing' around the primary crystallizing phases. Fig. 3 displays that three is no broad amorphous diffraction peak and some visible crystalline diffraction peaks appeared and were identified as CuZr and $Cu_{10}Zr_7$, respectively, so according to the expatiation above, it can be concluded that sample B consists of partial metallic glass matrix and a high volume fraction of primary crystallizing phases.

Moreover, due to further increase in the thickness of the plate, the microstructure of sample C would change successively. Fig. 2(c) shows more particles dispersed in the sample C and there is no particle gathering nearly with a limiting boundary like 'fencing'. There is still no broad amorphous diffraction peak and some visible crystalline diffraction peaks appeared (Fig. 3), which is similar to that of sample B. Those particles were identified as CuZr and $Cu_{10}Zr_7$ primary crystallizing phases too. So in the light of the analysis above, it can make sure that for sample C, there is nearly no metallic glass phase and its microstructure has been mainly changed into primary crystallizing phases.

Finally, for sample D, there are no small particles existing independently, as shown in Fig. 2(d), because the particles have congregated together into a new phase with a large size, identified as Zr_2Cu. Furthermore, Zr_2Cu was also detected in XRD patterns (Fig. 3). Meanwhile, the CuZr phase still remains, but the $Cu_{10}Zr_7$ phase disappears

completely. So in terms of the description above, one can ensure that for sample D, there is no any metallic glass phase existing yet, and its microstructure has changed into primary crystallizing phases completely.

In addition, Fig. 4 gives the DSC profiles of samples A, B, C and D. The sample A only exhibits one endothermic event, i.e., characteristics of the glass transition to a supercooled liquid state, followed by a distinct glass transition and undercooled liquid region. The glass transition temperature, T_g, the crystallization temperature, T_x and the extent of undercooled liquid region, ΔT_x (defined by $(T_x - T_g)$), are 705, 772 and 67 K, respectively, similar to the reported before [30]. But for sample B, the exothermic peak declines, indicating a dramatic decrease in the amount of metallic glass matrix. And the exothermic peak of sample C becomes very tiny, and even for sample D, its exothermic peak absolutely disappears. So based on the DSC data during crystallization in the current Cu–Zr–Al alloy, it is possible to calculate the volume fraction of the crystallization phases from enthalpy difference. Bian et al. [19] reported a method to evaluate the volume fractions of crystalline phases in Cu–Hf–Ti–Ag–Ta alloy by the following equation [31]:

$$\%V_{crys} = (\Delta H_{max} - \Delta H)/\Delta H_{max}, \quad (1)$$

where ΔH_{max} is the total enthalpy of transformation from the fully amorphous alloy to the completely crystallized alloy and ΔH is the enthalpy of the tested samples. DSC profiles of the samples with different thicknesses are shown in Fig. 4. It is obvious that the heat of crystallization decreases with the increase in the thickness. For sample A, its volume fraction of primary crystallizing phase should be equal to zero due to its fully amorphous structure. For samples B, C and D, their volume fractions of primary crystallizing phases were calculated to be about 29%, 95% and 100%, respectively. It is surprising that the sample B is only 2 mm thicker than the sample A, however, its volume fraction of primary crystallizing phase rises to 29%, indicating that the glass forming ability (GFA) is very sensitive to the cooling rate.

Finally, for samples A, B, C and D, due to their different thicknesses, the cooling rate during casting should be quite different accordingly. The cooling rate could be estimated from solution to the heat flow equation for a plate of liquid alloy cooled by heat conduction to a thick mold, which yields the following relation [32]:

$$R_C^{Plate} = 0.4K_t T_l / C_p L^2, \quad (2)$$

where K_t is the thermal conductivity, C_p is the specific heat of the alloy, T_l is the melting point, and L is the plate's thickness. Eq. (2) vividly shows that the cooling rate of the plate, R_C^{Plate}, has an inversely-proportional relationship with the square of thickness, L^2, indicating the cooling rate strongly depends on the thickness. To sum up, the increase in the thickness of the plate dramatically decreased the cooling rate, furthermore leading to the significant change of the microstructures.

3.2. Mechanical properties

Fig. 5 presents the compressive engineering stress–strain curves of samples A, B, C and D investigated, which elucidates the variation of yield strength, $\sigma_{0.2}$, fracture strength, σ_f and plastic strain, ε_p with the volume fraction of primary crystallizing phase, as listed in Table 1. It can be seen that sample A yielded at a stress, $\sigma_{0.2}$ of about 1.37 GPa and failed at a stress, σ_f of up to 1.99 GPa. But, its maximum strength, σ_b is about 2.06 GPa slightly higher than the fracture strength, σ_f. Its compressive plastic strain, ε_p, is up to 14.5%, which is quite close to the data reported by Das et al. [24]. For sample B, it yielded at a stress of about 1.41 GPa and its compressive strength reaches 1.92 GPa, that is equal to its fracture strength. Whereas, the plastic strain, ε_p is only 4.4%, similar to the reported before [33]. For sample C, it displays low elastic strain and then turns

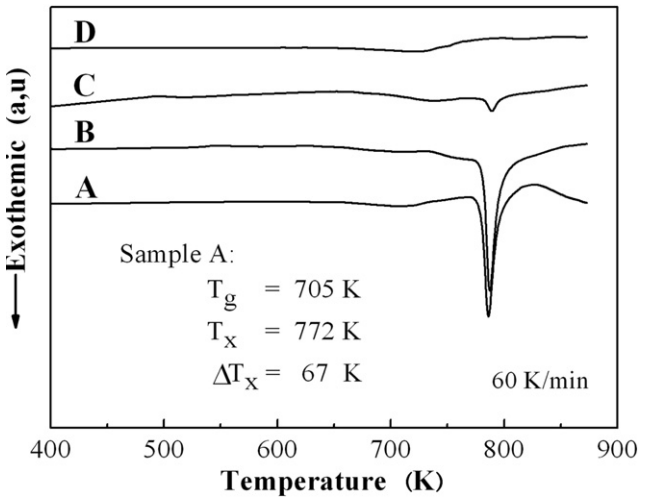

Fig. 4. DSC traces of $Zr_{47}Cu_{46}Al_7$ alloy for samples A, B, C and D at a heating rate of 60 K/min.

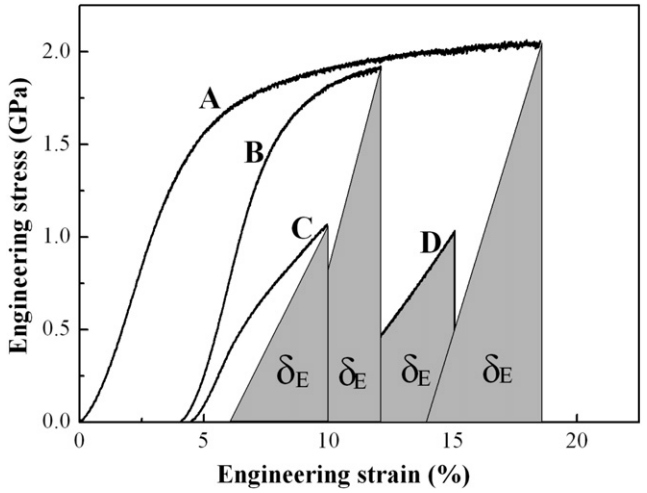

Fig. 5. Compressive engineering stress–strain curves of $Zr_{47}Cu_{46}Al_7$ alloy for samples A, B, C and D.

Table 1
Summary of the results of microstructures and mechanical properties of $Zr_{47}Cu_{46}Al_7$ alloy with different thickness

Sample no.	T (mm ± 0.01)	$\sigma_{0.2}$ (GPa ± 0.02)	σ_b (GPa ±0.02)	σ_f (GPa ± 0.02)	ε_p (% ± 0.02)	V_{crys} (% ±1)	Microstructure
A	2.3	1.37	2.06	1.99	14.5	0	Fully amorphous
B	4.2	1.41	1.92	1.92	4.4	29	Glass + CuZr + $Cu_{10}Zr_7$
C	6.4	–	1.07	1.07	–	95	CuZr + $Cu_{10}Zr_7$
D	8.3	–	1.03	1.03	–	100	CuZr + Zr_2Cu

into the second stage of so-called elastic deformation due to local cracking, at last catastrophically failed in a low stress level. For sample D, it only exhibits elastic deformation and then catastrophically failed in a low stress level of ~1 GPa. Fig. 6 shows the compressive true stress–strain curves of the four samples A, B, C and D. It seems that there is still no work-hardening behavior, but work softening, which is in contradiction to the report by Das et al. [24]. From the compressive properties of the four groups of samples, it can be concluded that the $Zr_{47}Cu_{46}Al_7$ metallic glass composites can exhibit significantly different mechanical properties due to the difference in their microstructures in detail although they have an identical composition.

3.3. Deformation and fracture morphologies

Figs. 7(a)–(c) show the deformation morphologies and shear fracture of sample A. It can be clearly seen that a primary crack runs through the whole surface, accompanied by another two short shear cracks, which terminate in the center of the sample (region I in Fig. 7(a)). The amplificatory photo (Fig. 7(b)) obviously shows that the three cracks are parallel to each other and the distances between them are about 160 and 120 μm, respectively. The compressive shear fracture angle, θ_c, between the stress axis and the fracture plane, is about 42°, as marked in the figure, i.e. smaller than 45°, which is in accord with the theoretical

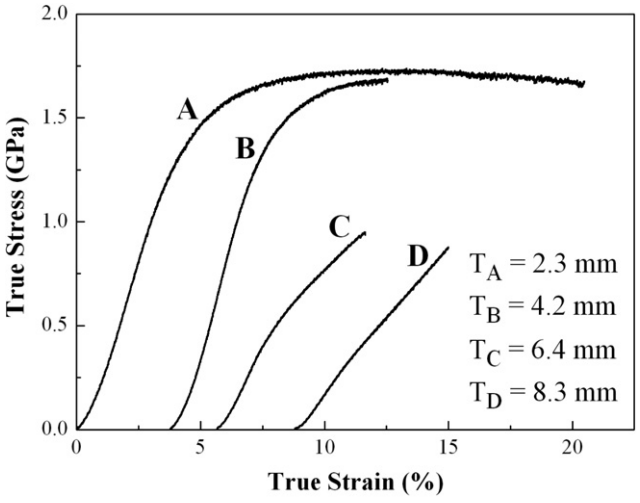

Fig. 6. Compressive true stress–strain curves of $Zr_{47}Cu_{46}Al_7$ alloy for samples A, B, C and D.

analysis by Zhang et al. [34]. Moreover, there are many long and parallel shear bands that are perpendicular to the primary crack, but it is noted that some shear bands become bending due to the rotation mechanism at a high compressive plasticity, according with the previous analysis [35] (region II in Fig. 7(a)). Fig. 7(c) demonstrates the local dense shear bands with a weaving structure in region II of Fig. 7(a) are in an equivalent distance nearly (Fig. 7(c)), similar to the report by Bei et al. [36]. Due to the formation of multiple shear bands along different directions, it is easy to understand why the sample A can display a very high compressive plasticity of about 14.5%.

Whereafter, further observations show that the vein-like pattern is widespread on the fracture surface, which is typical fracture feature for metallic glass (Fig. 7(d)). This vein-like pattern often extends along a uniform direction, as marked by arrows in the figure, which was explained by the local melting within the primary shear band induced by the high elastic energy in instantaneous fracture [37,38]. At the same time, the shear bands (or cracks) were observed to appear on the fracture surface with some steps covered by the molten liquid (Fig. 7(e)). Besides, it is interesting to find a peculiar feature with a mass of molten metallic glass liquid on the fracture surface (Fig. 7(f)). The molten metallic glass liquid seems to almost stuff the crack and there is some interspaces between the molten liquid and the edge of the crack, as indicated by arrow in Fig. 7(f), suggesting that the molten liquid should be extruded from the shear crack due to the local temperature rise inside with high pressure under compressive loading.

Figs. 8(a) and (b) show the shear fracture and shear bands on the surface of sample B. It is noted that the compressive fracture angle, θ_c, is approximately equal to 43°, as marked in the figure, i.e. smaller than 45° too. Besides, it is accidentally found that there is a long shear band parallel to the primary crack and the distance is about 190 μm (Fig. 8(b)). Moreover, there are also some long and continuous shear bands parallel to each other, which are perpendicular to the primary cracks on the whole (region II of Fig. 8(a)). It is suggested that those shear bands should contribute to the compressive plasticity of 4.4%, just as shown in Fig. 5. Afterwards, the further observations demonstrate that there are some different features on the fracture surfaces (Figs. 8(c)–(f)). Firstly, the vein-like pattern extends along a uniform direction, as marked by arrows in Fig. 8(c). Meanwhile, due to the friction during the compression fracture, the molten metallic glass liquid easily

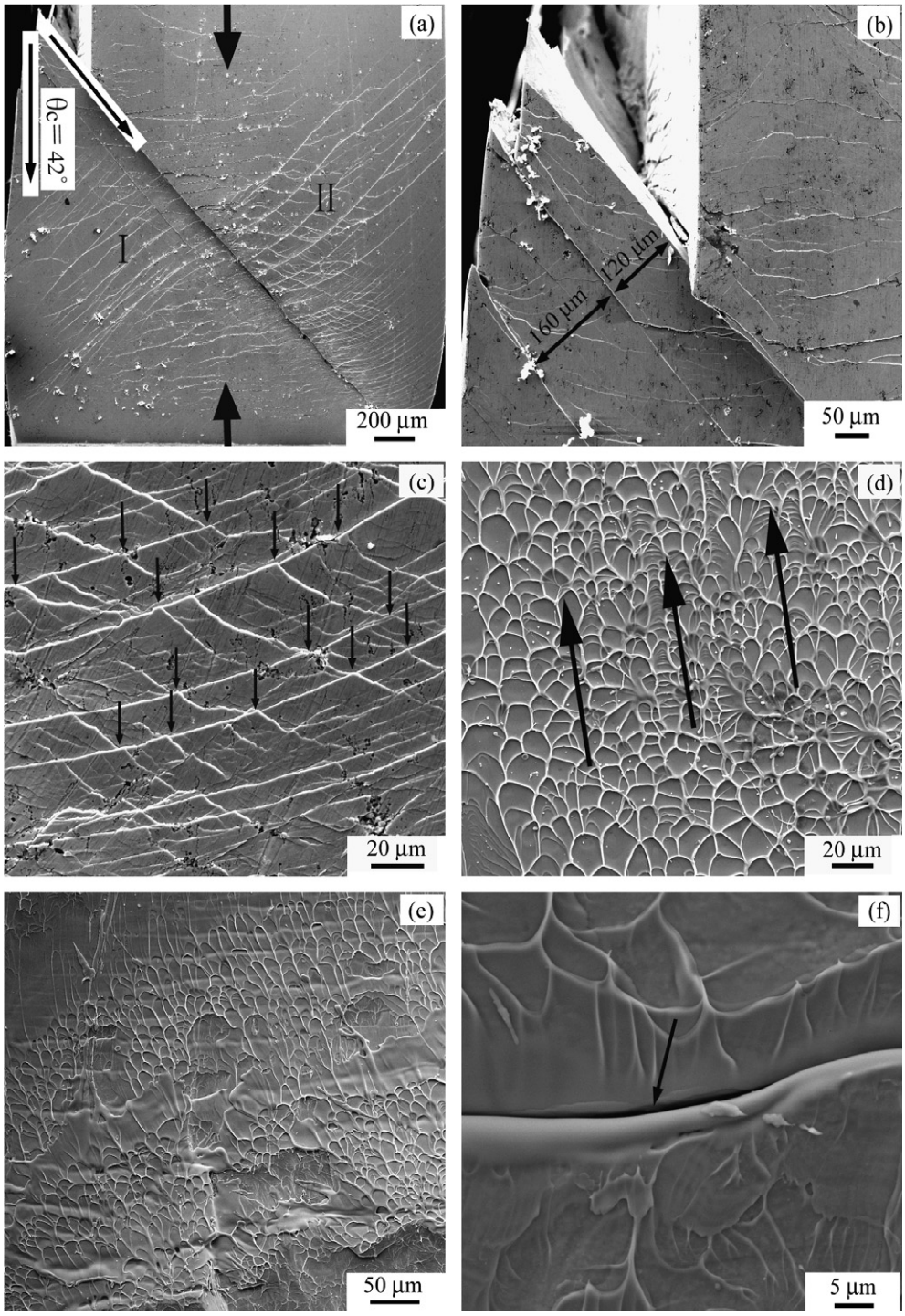

Fig. 7. SEM micrographs revealing the compressive fracture characters of sample A. (a–c) Shear bands on the specimen surface and (d–f) compressive fracture surfaces at different places.

flew and were piled up together as indicated by the circle. Secondly, Fig. 8(d) shows more abundant features at different regions on the fracture surface. For example, it is visible that the vein-like patterns and the molten traces appear in region I, and they are the typical features on the fracture surface of the metallic glasses [34,37–39]. In region II, there are some different microstructures with rough feature: many small holes embed in the rough surface, in which there are some particles with different size identified as the primary crystallizing phases (Fig. 8(e)). Finally, more primary crystallizing phases were found to congregate together in region III. Also, many dimples inside laying some grains were found at some local region (Fig. 8(f)). The observations above further indicate that the micro-

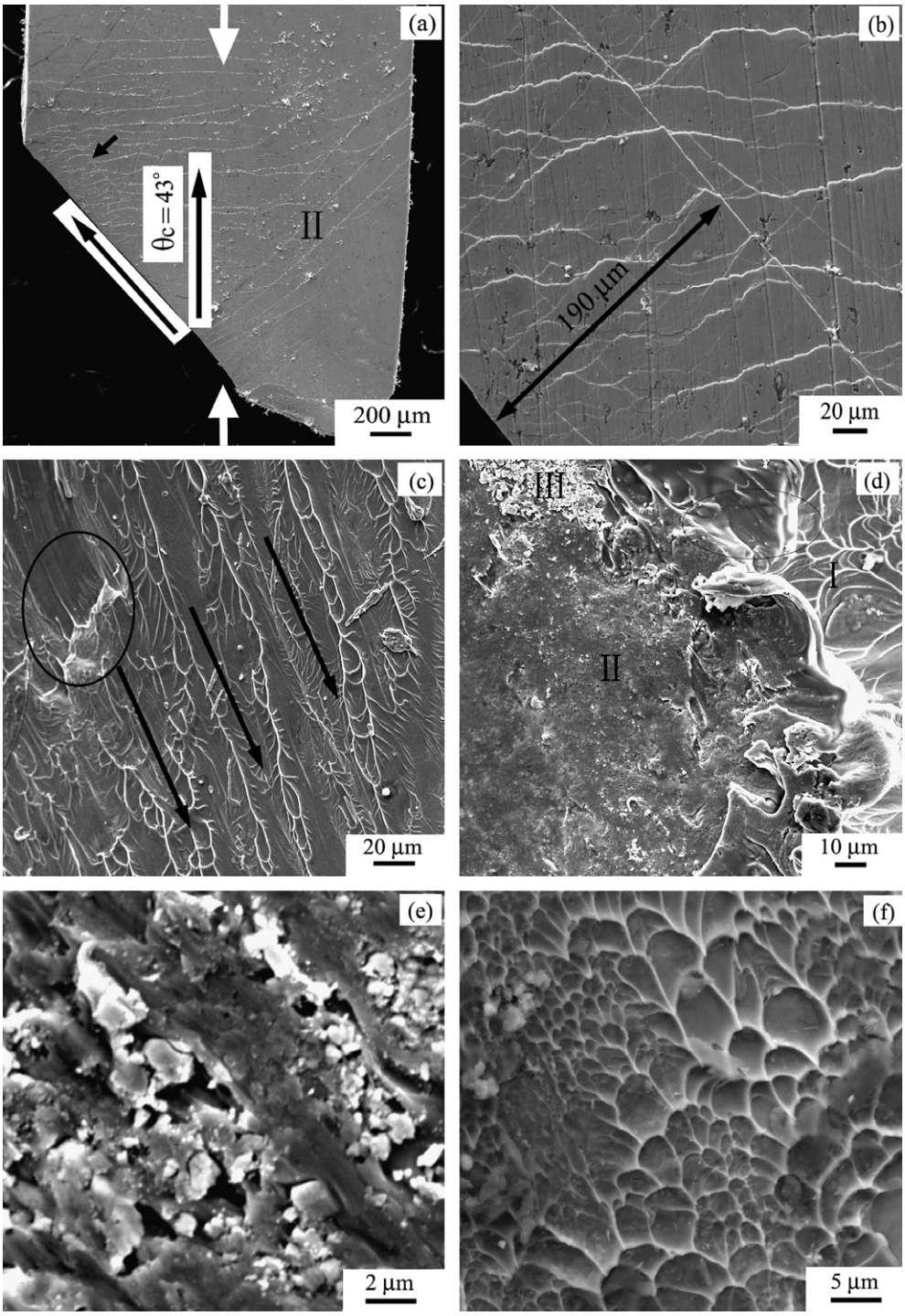

Fig. 8. SEM micrographs revealing the compressive fracture characters of sample B. (a, b) Shear bands on the specimen surface and (c–f) compressive fracture surfaces at different places.

structure of the sample B not only consists of metallic glass matrix failing in a shear fracture mode with the typical vein-like pattern, but also contains some primary crystallizing phases with a rough fracture feature.

Fig. 9(a) shows the compressive fracture feature of sample C. There is no visible shear band on the side surface and only are several irregular cracks, along which some edges have shed off and broken into pieces, as indicated by arrow. Except for the primary shear crack, there are two cracks parallel to the compressive stress axis indicating by the circles in the figure, apparently exhibiting a more brittle feature than the sample A or B, which is in accord with its compressive stress–strain curve. On the fracture surface, due to multiple cracks propagating together, many irregular cracks are clearly seen to wriggle across the surface, which results in a very rough fracture surface with a typical

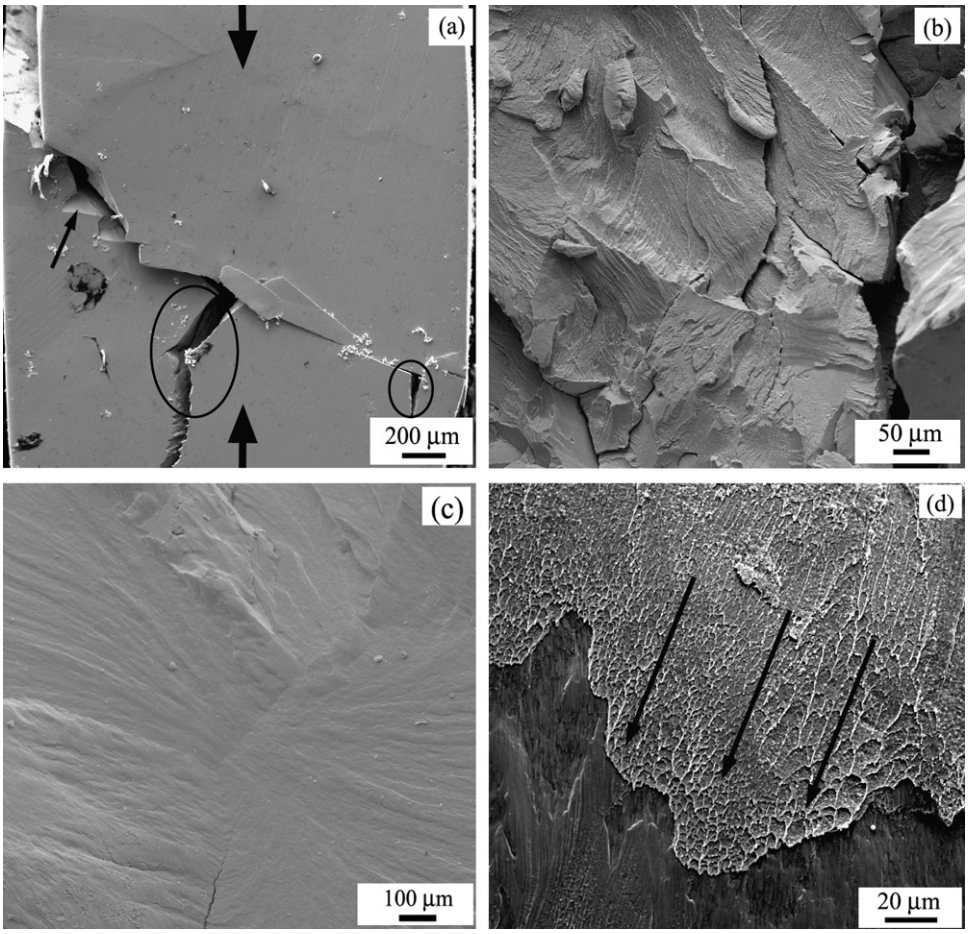

Fig. 9. SEM micrographs revealing the compressive fracture characters of sample C. (a) Brittle fracture side-surface and (b–d) compressive fracture surfaces at different places.

brittle feature (Fig. 9(b)). Meanwhile, at some regions, the fracture surface becomes very smooth (Fig. 9(c)), indicating a catastrophic failure with a rapid propagation of cracks or cleavage fracture. By careful observation, one can find that there is only a small area with the so-called vein-like pattern on the whole surface (Fig. 9(d)). The molten metallic glass liquid only appears at the edge of fracture surface due to the final shearing at fracture, similar to the observation in Fig. 8(f). The vein-like pattern seems to still contain some particles even though it extends along a uniform direction, as marked by arrows in the figure.

Fig. 10(a) shows the compressive fracture morphologies of sample D. There is still no any trace of shear band on the side surface and only a visible crack appears along a direction parallel to the compressive stress axis, as indicated by the ellipse in Fig. 10(a). Further observation on the fracture surface shows that there are some fracture ridges, which divide the fracture surface into several regions (Fig. 10(b)). Furthermore, at high magnification, some fracture dimples (or vein-like pattern) can also be clearly seen and some small particles are embedded in the dimples at local region (Fig. 10(c)). Moreover, it is also found that many primary crystallizing phases conglutinate into conglomeration (Fig. 10(d)).

4. Discussion

For the fully amorphous sample A, due to an isotropic microstructure, shear deformation approximately occurs along the maximum shear stress plane when subjected to a compressive load. So the main shear bands, initiating at the beginning of the plastic deformation, are parallel to each other (Figs. 7(a)–(c)). Meanwhile the shear bands also propagate along another maximum shear stress direction (Fig. 11(a)), leading to the grid patterns. The slight deviation of shear fracture angle, θ_c, from the maximum shear stress plane of 45° can be mainly attributed to the effect of the normal stress on the shear plane, as reported by Zhang et al. [34,39]. With further deformation, along the direction of primary shear bands, some short and sporadic shear bands would initiate in order to accommodate the strain induced by the primary shear bands, and even more shear bands would come out, forming multiple shear bands. At the same time, the primary shear bands would extend with the increase in plastic deformation (Fig. 11(b)) until turn into shear cracks (Fig. 11(c)). Always, the cracks seed from where the shear bands began and then propagated along them. As a result, these cracks are basically parallel to each other, the same with the par-

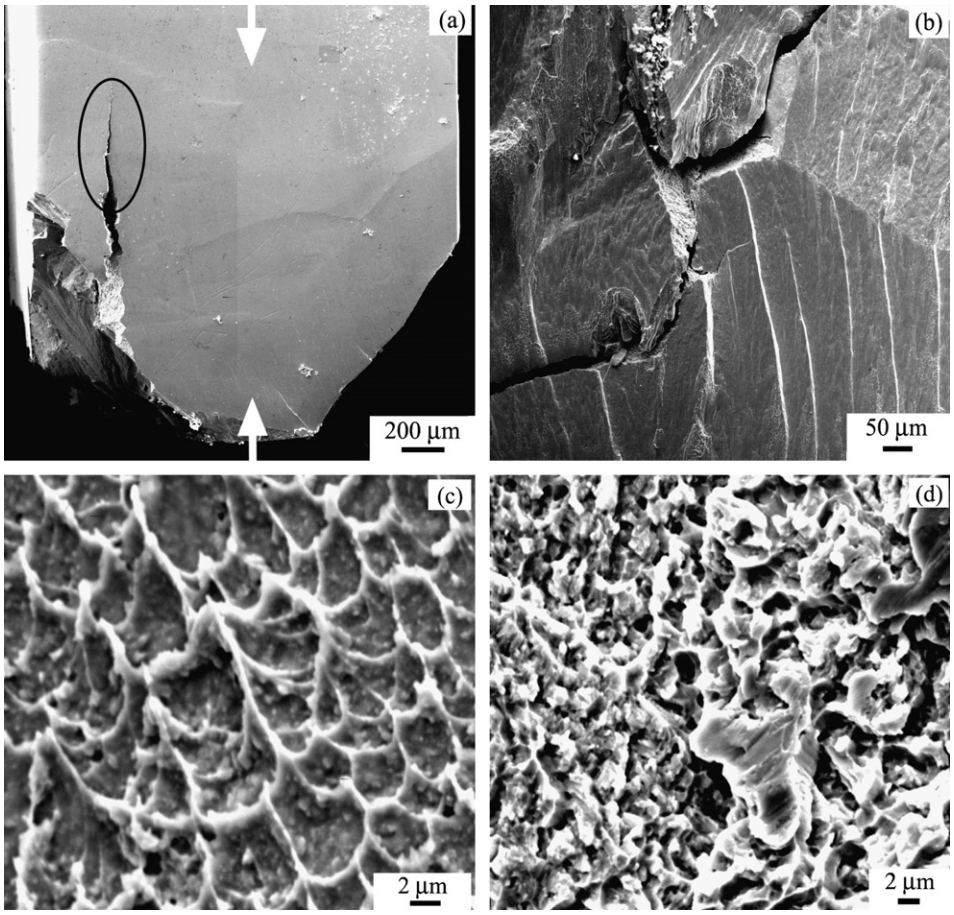

Fig. 10. SEM micrographs revealing the compressive fracture characters of sample D. (a) Brittle fracture side-surface and (b–d) compressive fracture surfaces at different places.

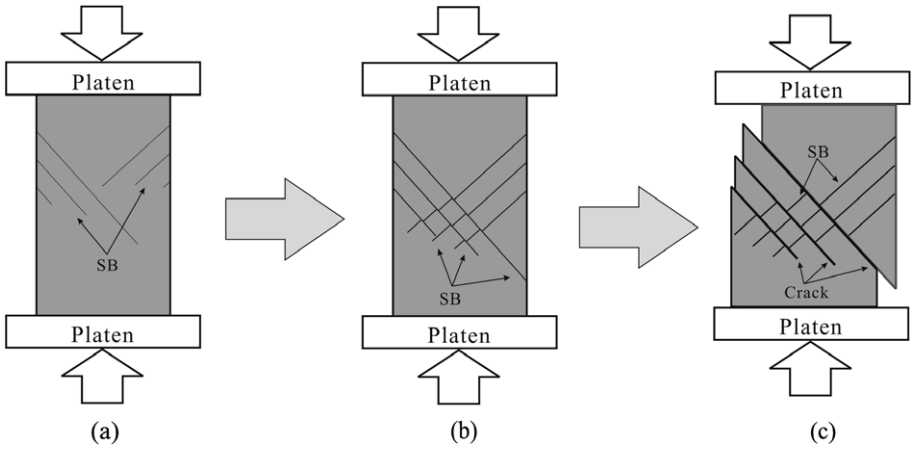

Fig. 11. Illustration of formation process of coarse primary shear bands and cracks.

allel shear bands. Because the directions of the two maximum shear stresses are perpendicular to each other approximately (Fig. 7(c)), the grid pattern often appears like ladder, as indicated by the arrows, similar to the report before [36]. Similarly, on the side-face of sample B, there are also some parallel shear bands along both directions of the maximum shear stress (Figs. 8(a) and (b)). This indicates that even though the volume fraction of primary crystallizing phase is up to 29%, its deformation behavior is still controlled mainly by the metallic glass matrix because the strength of metallic glass matrix is much higher than that of primary crystallizing phases. The sample C has a very low volume fraction of metallic glass phase, at first, its deformation behavior was still controlled by the metallic

Table 2
Energy density of $Zr_{47}Cu_{46}Al_7$ alloy with different thickness

Sample no.	T (mm ± 0.01)	δ_E (MJ/m^3 ± 0.5)	δ_P (MJ/m^3 ± 0.5)	δ_T (MJ/m^3 ± 0.5)	δ_E/δ_T (% ± 1)	δ_p/δ_T (% ± 1)
A	2.3	43	256	299	14	86
B	4.2	39	65	104	37	63
C	6.4	18	0	18	100	0
D	8.3	29	0	29	100	0

glass matrix, but once local cracks appeared, the consequent deformation behavior will be mainly dominated by the primary crystallizing phases, leading to a turning point in its compressive stress–strain curve (Fig. 6). For sample D, its volume fraction of primary crystallizing phases is up to 100% completely, thus, its deformation behavior must be fully controlled by the primary crystallizing phase, leading to a catastrophic failure.

Moreover, in comparison with the SEM micrographs of the compressive fracture characters of samples A, B, C and D, it can be clearly seen that the vein-like pattern and the melting liquid gradually disappear. For better understanding of such phenomenon, one can consider the effect of the elastic energy stored in the samples during compression [40]. As shown in Fig. 5, the area of the shadow triangle represents the elastic energy density δ_E, the area below the whole curve is the total energy density δ_T, and the plastic energy density δ_P is equal to their dispersion. So the three energy densities can be defined by the following three equations [40]:

$$\delta_T = \int_0^t \sigma \, d\varepsilon, \tag{3}$$

$$\delta_E = \sigma_f^2/2E, \tag{4}$$

$$\delta_P = \delta_T - \delta_E. \tag{5}$$

From the three equations above, we calculated the values of δ_E, δ_P, δ_T and δ_E/δ_T, which are listed in Table 2. It can be clearly seen that the plastic energy density, δ_P decreases sharply with the increase in the thickness, implying the energy consumed during compression decreases in the order of samples A, B, C and D.

For sample A, due to the continuous imposing of plastic strain energy into the sample, the local temperature within the primary shear band will increase and finally make the shearing layer soften during compression after yielding. Then the viscid liquid delayed the propagation of the shear cracks, leading to the formation of more secondary shear bands. Besides, the secondary shear bands not only relaxed a part of stress on the shear crack but also contributed to more plastic strain. It is slightly similar to the previous result that $Zr_{55}Al_{10}Ni_5Cu_{30}$ alloy exhibited 'work softening' due to the temperature- and stress-structure relaxation [41]. However, both the elastic density, δ_E and the plastic energy density, δ_P decrease with the increase in the thickness of the samples (Table 2), indicating an obvious reduction in local temperature. For sample B, the metallic glass matrix still plays an important role in the shear deformation at beginning, and contributes to its high strength and certain plasticity. The appearance of primary crystallizing phases, the disorder geometry, residual stress left inside and weak boundary, make the shear cracks seed and propagate much easier, which caused a sharp decrease in its plastic strain. Furthermore, for samples C and D, with very high volume fraction of primary crystallizing phases, due to their brittle nature and plentiful residual stress left, they displayed low compressive strength and without any plastic strain. And their fracture mode is very similar to that of the Fe-, and Co-based BMGs [42,43]. To sum up, for the $Zr_{47}Cu_{46}Al_7$ bulk metallic glass composites, their compressive deformation and fracture behaviors changed from ductility to brittleness with the increase in the volume fraction of primary crystallizing phases, depending on the microstructures completely. The final failure modes consist of typical shear fracture, splitting and even broken into several parts, i.e. fragmentation fracture, which were also observed in Fe-based BMG and Ti-based composites [43,44]. The investigations above further demonstrate that the BMG composites can display quite different mechanical properties and failure modes even for an identical alloy, due to the great change in the microstructures fabricated at different cooling rates.

5. Conclusions

For $Zr_{47}Cu_{a46}Al_7$ (at.%) alloy, it is found that its GFA or microstructure is strongly dependent on the plate thickness or cooling rate. With the increase in the cooling rate, the BMG composites are composed of different volume fraction of primary crystallizing phases. Furthermore, the deformation and fracture behaviors are dramatically affected by the volume fraction of primary crystallizing phases. For fully amorphous alloy, the deformation is controlled mainly by coarse shear bands and secondary shear bands, resulting in a high strength and a good plasticity of about 14.5% with a 'work softening' feature. However, with the increase in the amount of the primary crystallizing phases, the mechanical properties of BMG composites with different microstructures become deteriorated gradually even show a low compressive strength and completely brittle fracture. In short, the current investigation sheds light on that the mechanical properties of $Zr_{47}Cu_{46}Al_7$ alloy are sensitive to the cooling rate and can display completely different deformation and fracture behaviors and failure modes due to the great change in its microstructures.

Acknowledgements

The authors thank W. Gao, H.H. Su, J.L. Wen, G. Yao, and M.J. Zhang for mechanical tests, SEM and TEM observations. We thank Dr D.R. Fang for the help in the manuscript writing. This work is financially supported by the National Natural Science Foundation of China (NSFC) under Grant Nos. 50401019, 50501017, and 50625103, the 'Hundred of Talents Project' by the Chinese Academy of Science, and the Shenyang Center of Interfacial Materials (CIM).

References

[1] A.J. Drehman, A.L. Greer, D. Turnbull, Appl. Phys. Lett. 41 (1982) 716.
[2] T. Zhang, A. Inoue, T. Masumoto, Mater. Trans. JIM 32 (1991) 1005.
[3] A. Peker, W.L. Johnson, Appl. Phys. Lett. 63 (1993) 2342.
[4] A. Inoue, Acta Mater. 48 (2000) 279.
[5] W.L. Johnson, Mrs. Bull. 24 (1999) 42.
[6] F.Q. Guo, S.J. Poon, G.J. Shiflet, Appl. Phys. Lett. 84 (2004) 37.
[7] Z.P. Lu, C.T. Liu, Phys. Rev. Lett. 91 (2003) 115505.
[8] S. Yi, J.K. Lee, W.T. Kim, D.H. Kim, J. Non-Cryst. Solids 291 (2001) 132.
[9] W.H. Wang, H.Y. Bai, J. Appl. Phys. 84 (1998) 5961.
[10] Z.P. Lu, H. Tan, Y. Li, S.C. Ng, Scripta Mater. 42 (2000) 667.
[11] G. He, W. Löser, J. Eckert, L. Schultz, J. Mater. Res. 17 (2002) 3015.
[12] A. Inoue, T. Zhang, Mater. Trans. JIM 37 (1996) 185.
[13] K. Hashimoto, N. Kumagai, H. Yoshioka, H. Habazaki, A. Kawashima, K. Asami, B.P. Zhang, Mater. Sci. Eng. A 22&25 (1991) 133.
[14] H. Kato, T. Hirano, A. Matsuo, Y. Kawamura, A. Inoue, Scripta Mater. 43 (2000) 503.
[15] H. Choi-Yim, R. Busch, U. Köster, W.L. Johnson, Acta Mater. 47 (1999) 2455.
[16] C. Fan, R.T. Ott, T.C. Hufnagel, Appl. Phys. Lett. 81 (2002) 1020.
[17] J.C. Lee, Y.C. Kim, J.P. Ahn, H.S. Kim, S.H. Lee, B.J. Lee, Acta Mater. 52 (2004) 1525.
[18] C.C. Hays, C.P. Kim, W.L. Johnson, Phys. Rev. Lett. 84 (2000) 2901.
[19] Z. Bian, H. Kato, C.L. Qin, W. Zhang, A. Inoue, Acta Mater. 53 (2005) 2037.
[20] G. He, J. Eckert, W. Löser, L. Schultz, Nature Mater. 2 (2003) 33.
[21] G. He, W. Löser, J. Eckert, Acta Mater. 51 (2003) 5223.
[22] T.C. Hufnagel, C. Fan, R.T. Ott, J. Li, S. Brennan, Intermetallics 10 (2002) 1163.
[23] Z. Bian, G.L. Chen, G. He, X.D. Hui, Mater. Sci. Eng. A 316 (2001) 135.
[24] J. Das, M.B. Tang, K.B. Kim, R. Theissmann, F. Baier, W.H. Wang, J. Eckert, Phys. Rev. Lett. 94 (2005) 205501.
[25] Y.F. Sun, B.C. Wei, Y.R. Wang, W.H. Li, T.L. Cheng, C.H. Shek, Appl. Phys. Lett. 87 (2005) 051905.
[26] F. Jiang, Z.J. Wang, Z.B. Zhang, J. Sun, Scripta Mater. 53 (2005) 487.
[27] F. Jiang, Z.B. Zhang, J. Zhang, L. He, J. Sun, Acta Metall. Sin. 41 (2005) 1031.
[28] I.I. Konovalov, V.A. Komissarov, A.A. Maslov, V.K. Orlov, J. Non-Cryst. Solids 207 (1996) 536.
[29] D.H. Xu, G. Duan, W.L. Johnson, Phys. Rev. Lett. 92 (2004) 245504.
[30] J. Eckert, J. Das, K.B. Kim, F. Baier, M.B. Tang, W.H. Wang, Z.F. Zhang, Intermetallics 14 (2006) 876.
[31] T. Gloriant, A.L. Greer, Nanostruct. Mater. 10 (1998) 389.
[32] B. Lohwongwatana, J. Schroers, W.L. Johnson, Phys. Rev. Lett. 96 (2006) 075503.
[33] F. Jiang, Z.B. Zhang, L. He, J. Sun, H. Zhang, Z.F. Zhang, J. Mater. Res. 21 (2006) 2638.
[34] Z.F. Zhang, J. Eckert, L. Schultz, Acta Mater. 51 (2003) 1167.
[35] Z.F. Zhang, G. He, H. Zhang, J. Eckert, Scripta Mater. 52 (2005) 945.
[36] H. Bei, S. Xie, E.P. George, Phys. Rev. Lett. 96 (2006) 105503.
[37] W.J. Wright, R. Saha, W.D. Nix, Mater. Trans. 42 (2001) 642.
[38] C.T. Liu, L. Heatherly, D.S. Easton, C.A. Carmichael, J.H. Schneibel, C.H. Chen, J.L. Wright, M.H. Yoo, J.A. Horton, A. Inoue, Metall. Mater. Trans. 29 (1998) 1811.
[39] Z.F. Zhang, G. He, J. Eckert, L. Schultz, Phys. Rev. Lett. 91 (2003) 045505.
[40] X.F. Pan, H. Zhang, Z.F. Zhang, M. Stoica, G. He, J. Eckert, J. Mater. Res. 20 (2005) 2632.
[41] H. Kato, A. Inoue, H.S. Chen, Acta Mater. 54 (2006) 891.
[42] Z.F. Zhang, F.F. Wu, W. Gao, J. Tan, Z.G. Wang, M. Stoica, J. Das, J. Eckert, B.L. Shen, A. Inoue, Appl. Phys. Lett. 89 (2006) 251917.
[43] Z.F. Zhang, H. Zhang, B.L. Shen, A. Inoue, J. Eckert, Philos. Mag. Lett. 86 (2006) 643.
[44] Z.F. Zhang, G. He, J. Eckert, Philos. Mag. 85 (2005) 897.